Geophysical Research Letters

RESEARCH LETTER
10.1029/2021GL097471

Fluid-Kinetic Variations in the Storm-Time Inner Magnetosphere

Christopher C. Chaston[1]

[1]Space Sciences Laboratory, University of California, Berkeley, CA, USA

Key Points:

- Broadband low frequency electromagnetic fluctuations in the storm-time inner magnetosphere are decomposed as a superposition of fluid-kinetic modes
- Alfvénic modes on Magnetohydrodynamics (MHD) to kinetic scales dominate spectral composition with contributions from fast MHD, and slow MHD-kinetic modes
- Parallel phase speeds of the Alfvén and fast modes coincide over a broad range of frequencies suggestive of mode coupling/conversion

Supporting Information:

Supporting Information may be found in the online version of this article.

Correspondence to:

C. Chaston,
ccc@ssl.berkeley.edu

Citation:

Chaston, C. C. (2022). Fluid-kinetic variations in the storm-time inner magnetosphere. *Geophysical Research Letters*, *49*, e2021GL097471. https://doi.org/10.1029/2021GL097471

Received 14 DEC 2021
Accepted 12 APR 2022

Abstract Storm-time broadband electromagnetic field variations along the interface between the dipolar field of the Earth's inner-magnetosphere and the stretched fields of the plasma-sheet are decomposed as a superposition of fluid-kinetic modes. Using model eigen-vectors operating on the full set of Van Allen Probes fields measurements it is shown how these variations are composed of a broad spectrum of dispersive Alfvén waves with significant spectral energy densities in the fast and slow modes over scales extending into the kinetic range. These modes occupy volumes in k-space that define the field variations observed at each spacecraft frame frequency (f_{sc}). They are in aggregate not necessarily planar and often comprise filamentary structures with no distinct propagation direction in the perpendicular plane. Within these volumes the characteristic parallel phase speeds of the fast and Alfvénic modes coincide over a broad range of f_{sc} suggestive of coupling/conversion between modes.

Plain Language Summary Intervals of disturbed space weather, known as geomagnetic storms, inject energy in the form of electromagnetic (EM) fluctuations and energized particles deep into near-Earth space. During these times this region is pervaded by a broad spectrum of low frequency oscillations in EM fields that scatter/energize particles. In this research a novel technique utilizing the full set of fields measurements returned from the Van Allen Probes is applied to characterize the nature of these oscillations in terms of elemental plasma modes. The analysis reveals that a superposition of modes across a range of spatial scales is required to account for the oscillations at each frequency. It is described how this superposition is related to the filamentary morphology of the field structures encountered and demonstrated that coupling and/or conversion between the elemental plasma modes may occur. This work generalizes standard wave analysis approaches by describing fluctuations at a given spacecraft frame frequency as the integrated product of fluctuations over a range of wave scales and orientations rather than a single mode with specific wavelength, frequency and propagation direction.

1. Introduction

The collision of fast Earthward flows through the plasma sheet with the dipolar fields of the inner magnetosphere drive field and plasma compressions, shears, particle energization and plasma heating (Gabrielse et al., 2014; Liu et al., 2016, 2018; Runov et al., 2013). The electromagnetic energy transport and conversion processes at the center of these dynamics are mediated by the normal modes of the plasma. These modes describe the average relationship between the variations in the electromagnetic fields and bulk particle distributions (Kivelson and Russell, 1995). They characterize the energy transport through Poynting flux into and out of those regions where Earthward flows deposit energy as their inward motion is arrested (Angelopoulos et al., 2002). Identifying the nature of these variations in terms of the constituent plasma modes is therefore necessary to characterize the flow of energy from the plasma sheet into the inner magnetosphere, ionosphere, and upper atmosphere (Dombeck et al., 2005; Hull et al., 2020; Keiling et al., 2002; Tian et al., 2021; Wygant et al., 2000).

Observations from the Van Allen Probes have demonstrated the prevalence of broad-spectrum electromagnetic fluctuations along the interface between the dipolar field-lines of the inner magnetosphere and tail-like field-lines extending outward into the plasma sheet (Chaston et al., 2014, 2015; Hull et al., 2019; Malaspina et al., 2015; Moya et al., 2015). An illustrative example recorded during the geomagnetic storm of 1 June 2013, observed from Van Allen Probe A is shown in Figure 1. Here, broad-spectrum fluctuations in electromagnetic fields (Figures 1b–1e), particularly during storm main phase (Figure 1a), dominate the spectrum from 0.01 to 10 Hz in the spacecraft frame. The variation in the spectral energy density as a function of time, or spacecraft location, is synchronous with changes in the energetic fluxes in both ions and electrons shown in Figures 1f

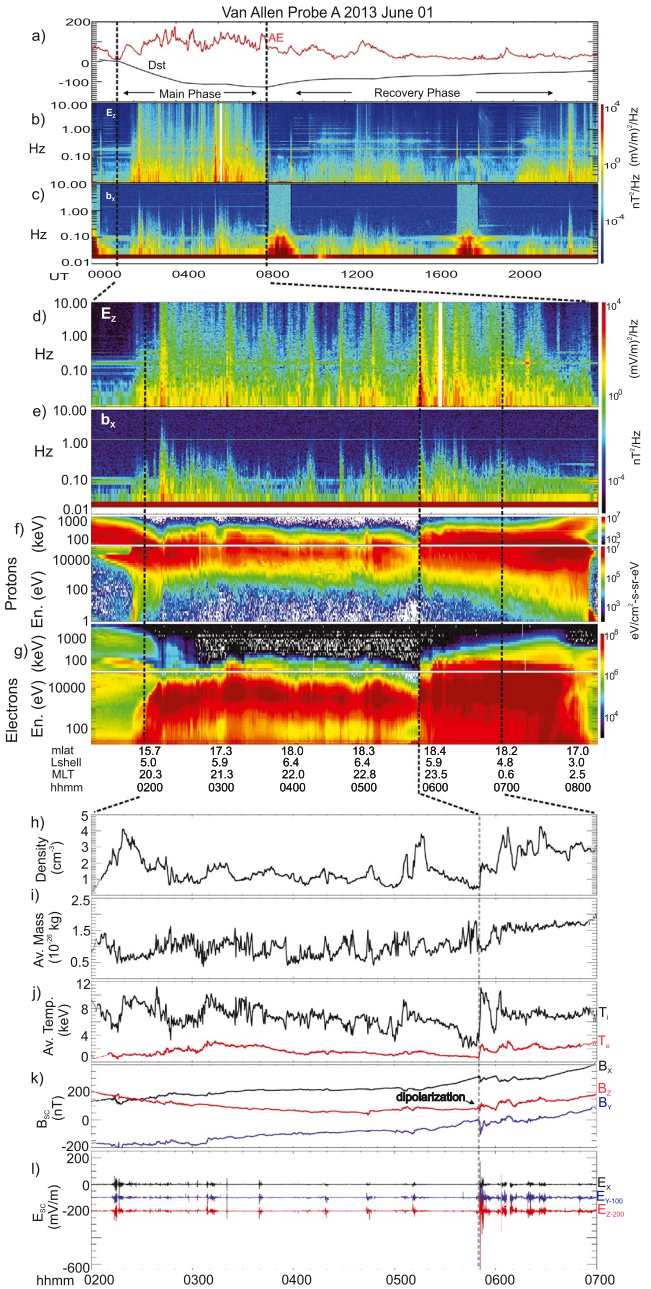

Figure 1. Storm-time observations from Van Allen Probe A, 1 June 2013. (a) Dst (Disturbance Storm Time) and AE (Auroral Electrojet) indices. (b–e) low frequency electric and magnetic field spectrograms from EFW and EMFISIS—components are in spacecraft coordinates as defined in the text. (f, g) Proton and electron omni-directional differential energy flux spectrograms from MAGEIS and HOPE. (h–j) Density, average ion mass, and average temperatures from HOPE. (k, l) magnetic and electric field (Earth's frame) vectors in spacecraft coordinates.

and 1g respectively. This synchronicity is symptomatic of the coupling of large scale Magnetohydrodynamics (MHD) plasma compressions and flows to intermediate and kinetic scale broad-band field variations. Figures 1h–1l capture these variations in a reduced set of parameters to be analyzed in the main body of this report.

The broad-band fluctuations along this interface have been characterized as part of an Alfvénic cascade delivering energy to kinetic scales to drive ion and electron energization and scattering (Chaston et al., 2015; Hull et al., 2020). This characterization is based on the relative magnitude of spectral energy densities in transverse electric and magnetic fields that follow the expected scale dependent impedance relations for dispersive Alfvén waves. While this model is consistent with the transverse variations observed, it is often the case that simultaneous compressive variations are observed on intermediate scales that are not necessarily in agreement with a purely Alfvénic description (Chaston et al., 2015; Malaspina et al., 2015). Indeed, flows in the near-Earth plasma sheet are thought to launch fast mode waves Earthward (Kepko et al., 2001; Saito et al., 2008) while dipolarization fronts have a slow-mode-like character (Runov et al., 2011) and fluctuations within flows trailing these fronts have been interpreted as slow mode waves (Wang et al., 2016). Plasma structures here have a diamagnetic character suggestive of interchange/ballooning instability in the generation of turbulence in the near-Earth plasma sheet (Cheng & Zaharia, 2004; Miura et al., 1989; Panov et al., 2012; Panov & Pritchett, 2018; Pritchett & Coroniti, 2010; Roux et al., 1991). Furthermore, inhomogeneities along the interface between inner magnetospheric and stretched plasma-sheet field-lines during disturbed times infer that mode coupling and conversion should occur here (Allan & Wright, 2000; Lysak et al., 2009). These considerations demand additional analyses of field and plasma variations in this critical region of near-Earth space to characterize the spectral composition more completely.

Here, a technique that decomposes the full set of observed field variables from the Van Allen Probes into the constituent normal modes of the plasma at frequencies below the ion cyclotron frequency (Ω_i) is applied. This is performed over a range of scales extending from those of MHD deep into the kinetic range. The analysis is implemented using a background plasma model that varies with the scale of the fluctuations enabling the characterization of 3-D time variant structures on plasma gradients as the superposition of linear modes populating volumes in k-space.

2. Fluid-Kinetic Analysis Technique

The basis for performing an analysis of the broad-spectrum electromagnetic fluctuations observed from the Van Allen Probes is a plasma model that appropriately describes the fluctuations over the observed range of spatial and temporal scales. Following previous analyses of these observations (Chaston et al., 2014), fluctuations for which $\omega < \Omega_i$ are considered and described using a fluid-kinetic model (Hollwegg, 1999) on scales extending from MHD down to sub ion-gyro radii. In this model kinetic effects due to finite perpendicular scale are included in a "fluid" formalism that provides wave properties in agreement with those derived from a full kinetic treatment with the omission of wave damping (Cheng & Johnson, 1999; Lysak & Lotko, 1996). Analysis of the model equations for an isotropic plasma provides the dispersion relation,

$$\left(\frac{\omega^2}{k_z^2 v_A^2} - 1\right)\left[\omega^2\left(\omega^2 - k^2 v_A^2\right) - \beta k^2 v_A^2\left(\omega^2 - k_z^2 v_A^2\right)\right] = \omega^2\left(\omega^2 - k^2 v_A^2\right) k_y^2\left(\rho_s^2 + \rho_i^2\right) \quad (1)$$

where ω is the wave frequency, v_A is the Alfvén speed, $\beta = \mu_o n_0 (T_e + T_i)/B_0^2$ and $\rho_s = \sqrt{T_e/m_i}/\Omega_i$ and $\rho_i = \sqrt{T_i/m_i}/\Omega_i$ are the ion acoustic and ion gyro-radii respectively. Here n_0 and B_0 are the slowly varying plasma density and total magnetic field strength, T_e and T_i are the electron and ion temperatures and m_i is the ion mass. Note that contributions due to electron inertia are ignored since locally $\frac{v_e}{v_A} \gg 1$. The wavevector in field-aligned coordinates is $\boldsymbol{k} = (0, k_y, k_z)$ with z along $\boldsymbol{B}_0$. At each location in k-space Equation 1 provides 6 solutions corresponding to the Alfvén, fast and slow modes propagating along (forward, $\boldsymbol{k}_z \cdot \boldsymbol{B}_0 > 0$) and opposite to (backward, $\boldsymbol{k}_z \cdot \boldsymbol{B}_0 < 0$) $\boldsymbol{B}_0$. The normalized phase speeds (ω/kv_A) of these modes as function of wave-normal angle (θ_k) and $k_y\rho_i$ for a proton-electron plasma representative of those observed is shown in Figures 2a–2c. These panels apply to both forward and backward modes. On large transverse scales (small $k_y\rho_i$) these solutions describe the classical non-dispersive MHD modes that transition into the corresponding kinetic modes as $k_y\rho_i$ increases. The field components of these modes facilitate the formation of eigenvectors which can be used to "filter" the observed fluctuations and estimate the contribution of each mode to the total spectral energy density (ε) observed. This approach has been described for MHD fluctuations by Glassmeier et al. (1995).

Over the frequency range of interest, the Van Allen Probes provide the electric field vector in the spacecraft spin plane (E_{ysc}, E_{zsc}) and the full magnetic field vector (b_{xsc}, b_{ysc}, b_{zsc}) (Kletzing et al., 2013; Wygant et al., 2013). Here x_{SC} is normal to the spacecraft spin plane and points toward the Sun, y_{SC} lies along the projection of the ecliptic plane into the spacecraft spin plane and retrograde to planetary motion, while z_{SC} completes the right-handed set. In addition, density moments are provided by the plasma instrument onboard the Van Allen Probes (Funsten et al., 2013), however these are not of sufficient cadence to provide the fluctuating density (nor fluctuations in the flow) for this study. Higher cadence density measurements could be estimated from the spacecraft potential (Jahn et al., 2020), however, close to apogee during storm times interpretation of these voltages as density fluctuations requires verification. The variations at each time (t) and spacecraft frame frequency (f_{sc}) are therefore described by a reduced state vector defined in spacecraft coordinates as,

$$\boldsymbol{\vartheta}(f_{sc}, t) = \frac{1}{v_A}\left[\frac{E_{ysc}(f_{sc}, t)}{B_0}, \frac{E_{zsc}(f_{sc}, t)}{B_0}, \frac{b_{xsc}(f_{sc}, t)}{\sqrt{\mu_o \rho}}, \frac{b_{ysc}(f_{sc}, t)}{\sqrt{\mu_o \rho}}, \frac{b_{zsc}(f_{sc}, t)}{\sqrt{\mu_o \rho}}\right] \quad (2)$$

where ρ is the background mass-density. The corresponding partial eigenvectors ($\boldsymbol{e}$) for each mode are derived from the solutions of Equation 1 using the relations for E and b defined in the Supporting Information. These model-field vectors are defined in the field-aligned coordinate system for a given $\boldsymbol{k}$ and rotated into spacecraft coordinates using the projection of $\boldsymbol{k}$ into this system ($\boldsymbol{k}_{sc}$) to form $\boldsymbol{e}$. The fraction of ε attributed to each mode (i) is then provided by the matrix equation,

$$\overline{g}_i(f_{sc}, t) = \boldsymbol{e}_i S(f_{sc}, t)\, \boldsymbol{e}_i^{\dagger} / \varepsilon(f_{sc}, t) \quad (3)$$

where $S(f_{sc}, t) = \boldsymbol{\vartheta}^{\dagger}\boldsymbol{\vartheta}$ is the full observed spectral matrix, $\varepsilon(f_{sc}, t) = Tr[S(f_{sc}, t)]$, $\boldsymbol{e}_i$ is the model-defined complex unit partial eigenvector of the ith mode, and $\dagger$ and Tr respectively denote Hermitian adjoint and trace. If $\boldsymbol{k}_{sc}$ is known for each mode at each (f_{sc}, t) then $\overline{g_i}(f_{sc}, t)$ can in principle be evaluated from Equation 3.

The omission of the variations in particle pressure in the formulation of $\boldsymbol{\vartheta}$ reduces the capacity to distinguish modes in the plasma. To quantify "leakage" between modes Figures 2d–2f show the inner product $\boldsymbol{e}_i \cdot \boldsymbol{e}_j{}^{\dagger}$ evaluated using normalized partial eigenvectors corresponding to the solutions shown in Figures 2a–2c in spherical coordinates (k, θ_k and ϕ_k). The azimuthal angle (ϕ_k) is measured in a right-hand sense around $\boldsymbol{B}_0$ between the x-direction in field-aligned (FAC) coordinates and the direction of $k_\perp$. x_{FAC} in the $\boldsymbol{SC}$ system lies along the vector, $\left[-B_{0x}B_{0z}, -B_{0y}B_{0z}, {B_{0x}}^2 + {B_{0y}}^2\right]$, with z_{FAC} along $\boldsymbol{B}_0$. Here, $\boldsymbol{B_0}$ is taken to lie in the $x_{SC} - z_{SC}$ plane and inclined 45° to both coordinate axes to represent orientations during storm-times near apogee and local midnight from the Van Allen Probes. Alternate orientations provide comparable results. Values of zero in Figures 2d–2f indicate orthogonality with no "leakage" between modes, while values of one indicate that the modes cannot be distinguished using the state vector alone at that location in k-space. Based on this calculation it would seem possible to distinguish the Alfvén mode from the fast and slow modes over most of the volume shown with additional constraints required to distinguish the fast from slow mode.

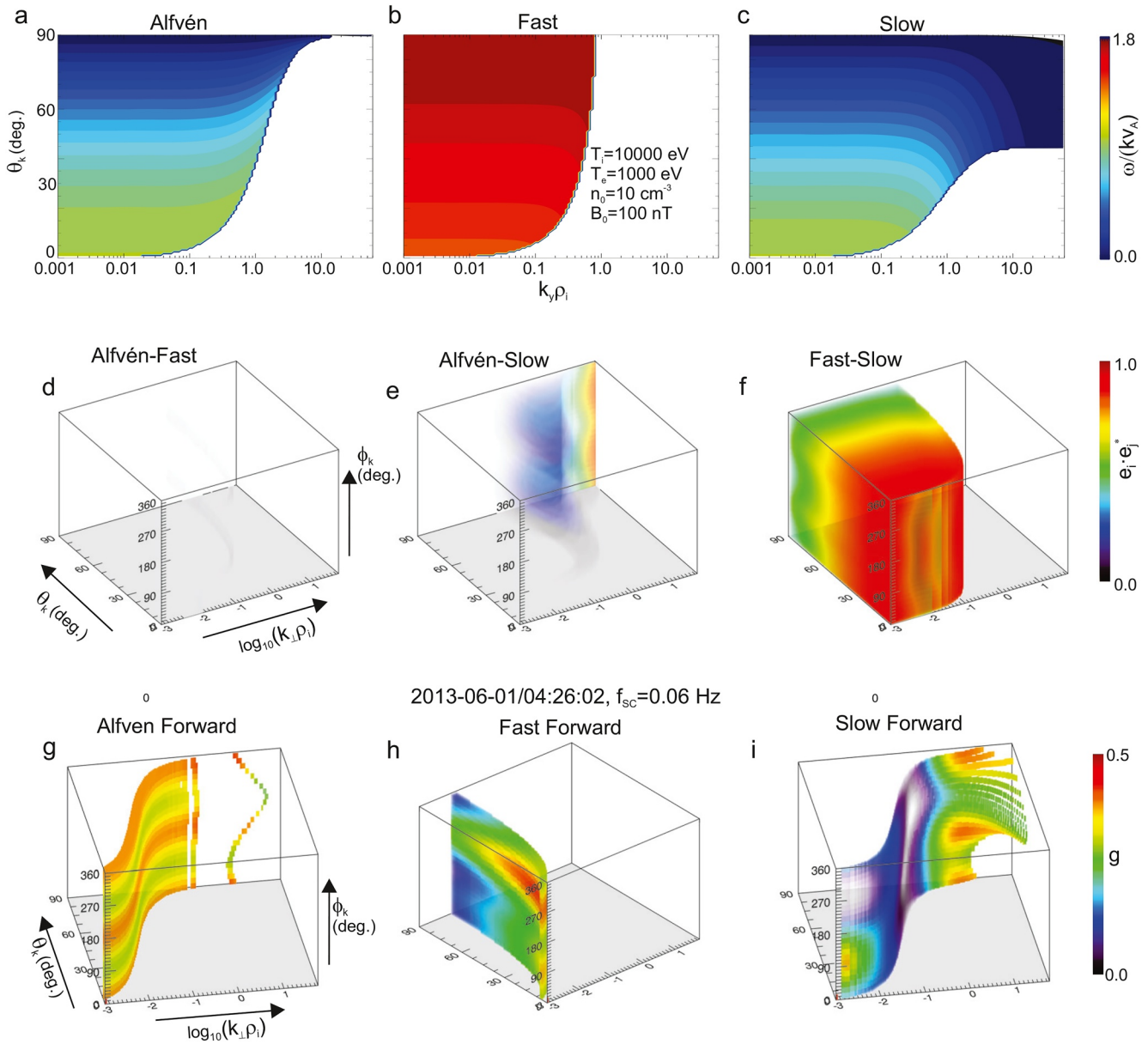

Figure 2. (a–c) Normalized phase speeds (ω/kv_A) of the Alfvén, fast and slow modes for the plasma model indicated as a function of wave-normal angle (θ_k) and normalized perpendicular wavenumber ($k_\perp\rho_i$). Inner product of eigenvectors as a function of θ_k, $k_\perp\rho_i$ and the azimuthal angle, ϕ_k, for the modes indicated. (g–i) $\overline{g}_i\,(k_\perp\rho_i, \theta_k, \phi_k\,)$ within volume V_k for each mode at the f_{SC} and time indicated.

The additional constraints are supplied by the differences in the mode phase speeds apparent in Figures 2a–2c. These speeds determine f_{SC} at which a mode at a given ω and $\boldsymbol{k}$ may appear. This frequency is,

$$f_{SC} = |\omega - \boldsymbol{k}_{SC} \cdot \boldsymbol{v}_{SC}|/2\pi \tag{4}$$

where $\boldsymbol{v}_{SC}$ is the velocity of the spacecraft through the plasma. For the broad spectra and flows measured from the Van Allen Probes, $\varepsilon\,(f_{SC}, t)$ at each f_{SC} and t will have contributions over the range of ω and $\boldsymbol{k}_{SC}$ that satisfy Equation 4. For this case the integrated composition can be defined as,

$$G_i\,(f_{SC}, t) = \frac{1}{V_k}\int \boldsymbol{e}_i S\,(f_{sc}, t)\,\boldsymbol{e}_i^{\dagger} dV_k \tag{5}$$

where $dV_k = {k_l}^2 \sin(\theta_k)\, d\theta_k d\phi_k dk_l$, k_l is log k for a logarithmic grid in k, and the integral is performed over the volume (V_k) in k-space where Equation 4 is satisfied for each wave mode (i). The normalized composition is then $\overline{G_i}(f_{SC}, t) = \boldsymbol{G}_i(f_{SC}, t) / \sum_i \boldsymbol{G}_i(f_{SC}, t)$.

Within V_k, a characteristic ω and $\boldsymbol{k}_{SC}$ may be identified at that location in k-space where $\overline{g}_i(f_{sc}, t)$ is largest. This can be located by searching V_k for minima of the function,

$$A_i(\boldsymbol{k}_{SC}) = 1 - \overline{g}_i(f_{SC}, t) \tag{6}$$

much in the manner of k-filtering (Motschmann et al., 1998) with the "filter" defined by the mode eigen-vector $\boldsymbol{e}_i$. Here it is noted that for the broad-spectrum fluctuations observed, $\boldsymbol{k}_{SC}$ of the characteristic mode will not necessarily coincide with that returned by a priori assuming a single plane wave at each f_{sc} and t and deriving $\boldsymbol{k}/\omega$ using Faraday's law (e.g., Santolik et al., 2003).

3. Storm Time Composition

The measurements required to perform this analysis over the "main phase" of the storm of Figure 1 are presented in Figures 1h–1l. Estimates for the spectral coefficients at each f_{SC} required to populate ϑ are derived using Morlet wavelets (Torrence & Compo, 1998) applied to the full magnetic field vector and the Y_{SC} and Z_{SC} electric field components in the rest frame of Earth (Figures 1k and 1l). The background plasma parameters ($\boldsymbol{B}_0, n_0, m_i, T_i, T_e, \boldsymbol{v}_{SC}$) at each wavelet scale are defined by low-pass filtering as $f_{SC} \leq 1/\alpha\tau_s$ where $\tau_s \approx \sqrt{2}/f_{SC}$ is the wavelet e-folding time. Values of $\alpha = 2 - 7$ provide nearly identical results and here $\alpha = 2$ is used. In advance, it is also noted that variations in the background parameters of up to 50% cause less than ~10% variation in composition (Chaston, Bonnell, Bale, et al., 2020). The spacecraft spin plane electric field measurements along with the axial component (E_{xsc}) given by the approximation $\boldsymbol{E} \cdot \boldsymbol{B}_o = 0$ are used to estimate $\boldsymbol{v}_{SC}$. For demonstration purposes, Figure 1l includes E_{xsc} derived in this manner with $\boldsymbol{B}_o$ defined by low pass filtering the magnetic field vector to $f_{SC} < 0.001$ Hz. The velocity of the spacecraft through the plasma is then $\boldsymbol{v}_{SC} = \boldsymbol{v}_{0\_SC} - (\boldsymbol{E} \times \boldsymbol{B}_o) / {B_0}^2$ where $\boldsymbol{v}_{0\_SC}$ is the orbital velocity. In practice, $\boldsymbol{v}_{SC}$ is derived at each wavelet scale and time for use in conjunction with the dispersion results to define V_k via Equation 4 for each mode at each f_{SC} and t. Each bin in f_{SC} has width Δf_{SC}, and all those k-space grid locations that satisfy Equation 4 over the range $f_{SC} \pm \Delta f_{SC}/2$ are included in V_k.

To illustrate how the analysis proceeds, Figures 2g–2i show $\overline{g_i}(k_\perp \rho_i, \theta_k, \phi_k)$ within V_k for each of the forward propagating modes at $f_{SC} = 0.06$ Hz and time 04:26:02 UT. Figure 2g shows that $\overline{g_i}$ for the Alfvén mode is broadly distributed in k and balanced in ϕ_k with peaks at ~180° and ~360° and "soft" maxima occurring at $k_\perp \rho_i \sim 1$ and $\theta_k \to 90^o$. The distribution of $\overline{g}_i$ in k-space for the other modes is more localized, however multiple maxima with similar peak values are apparent. These distributions indicate that the fluctuations are not well described as a single Fourier mode at a specific wavenumber. This non-specificity is replicated at each f_{SC} and t throughout this storm interval. Integration of these distributions, as defined by Equation 5, provides the corresponding mode composition results presented in Figure 3.

Figures 3a and 3b show the power spectra of the magnetic and electric field variations. The black regions in Figure 3b correspond to the digitization noise floor of the fluxgate magnetometer that constrains the frequency range for analysis. The normalized integrated composition over this range, $\overline{G_i}(f_{SC}, t)$, as defined by Equation 5 and the ratio of forward to backward composition, $\overline{G}(f_{SC}, t)_{\text{Forward}} / \overline{G}(f_{SC}, t)_{\text{Backward}}$, is presented in Figures 3c–3k. Note that these results provide continuous coverage from the MHD range through to kinetic scales where $k_\perp \rho_i > 1$.

Comparing Figures 3c–3k indicates a composition dominated by Alfvénic modes (Figures 3c and 3d) with a preference for propagation in the forward sense represented by the preponderance of red shading in Figure 3e. For the magnetic field orientation and the location of the Van Allen Probes at this time, this result corresponds to propagation, or energy transport, in the Alfvén mode along $\boldsymbol{B}_o$ primarily toward the northern ionosphere. There is however a significant flux in backward propagating Alfvén modes whose composition is at times anti-correlated with the forward mode in f_{SC} and t. The simultaneous presence of spectral energy densities in both the forward and backward modes is indicative of counter propagation and/or consistent with the presence of

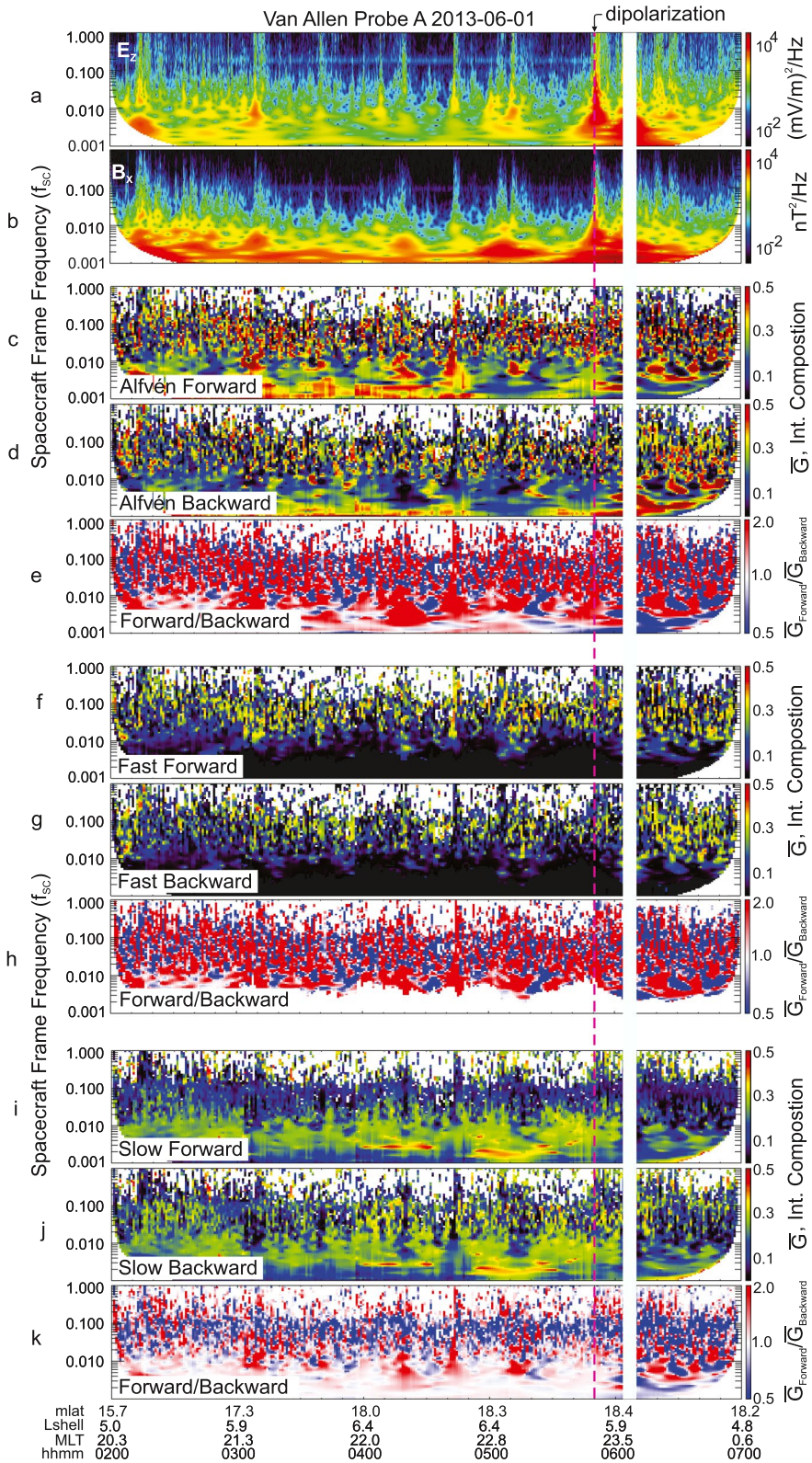

Figure 3. Fluid-kinetic mode composition. (a, b) Morlet wavelet spectrograms of the low frequency electric and magnetic field variations for the components indicated. (c–k) $\overline{G_i}\,(f_{SC},t)$ (normalized total composition) and $\overline{G}\,(f_{SC},t)_{Forward}\,/\overline{G}\,(f_{SC},t)_{Bckward}$ for each mode.

field-line eigenmodes identified from the Van Allen Probes in previous studies (Chaston et al., 2014). Significantly, the contribution from the backward mode at the lowest frequencies becomes largest after 0550 UT following the dipolarization of the magnetic field (Figure 1k).

Figures 3f and 3g show significant contributions from the fast mode throughout the interval at $f_{SC} \geq 0.01$ Hz. There is a preference for propagation in the forward direction along $\boldsymbol{B}_0$ (Figure 3h). The fast mode effectively disappears from the composition for $f_{SC} \lesssim 0.01$ Hz over which range the compressional field variations are dominated by the slow mode (Figures 3i and 3j). In fact, comparison of Figures 3f and 3g to Figures 3i and 3j shows that slow and fast mode spectral energy densities are anti-correlated. For $f_{SC} \lesssim 0.01$ Hz the slow mode shows no persistent preference for forward or backward propagation along $\boldsymbol{B}_o$, but above this frequency this mode is preferentially found in the backward sense (Figure 3k). This suggests a source located closer to the northern ionosphere. After the field dipolarization there is a progressive decrease and increase in the slow mode and fast mode composition respectively.

4. Wave Properties

While the composition results described above are defined by integration over V_k, it is instructive to consider the characteristic wave properties at the minima in A_i ($\boldsymbol{k}_{SC}$) within V_k at each f_{SC} and t. Figure 4 shows these properties for the forward modes, noting that the results for the backward modes are qualitatively similar. For context the average ion temperature (~6 keV), mass ($\sim 10^{-26}$ kg) and magnetic field (~300 nT) provide a thermal ion gyro-radius of ~90 km so that $k_\perp \rho_i = 1$ at $k \sim 1 \times 10^{-5}$. Values of k at, and above, this wavenumber, correspond to the kinetic range and are represented in Figures 4a, 4e and 4i by yellow to red shading.

Figure 4 shows that the characteristic wavevectors (Figure 4a) for the Alfvén mode span the range from MHD scales well into the kinetic range at largest f_{SC}. These wavevectors are highly oblique with wave-normal angles (Figure 4b) approaching 90° over the frequency range shown. This result is consistent with those returned via fits of impedance relations for kinetic Alfvén waves to the observed electromagnetic wave spectra where $k_\perp \sim 2\pi f_{SC}/v_{SC}$ (Chaston et al., 2015). Plasma frame wave frequencies (ω) (Figure 4c) increase with f_{SC} with values normalized by the ion gyrofrequency (ω/Ω_i) generally much less than one. There also appears to be no definitive orientation for $k_\perp$; ϕ_k varies erratically over the full 2π radians in the perpendicular plane (Figure 4d).

In contrast, the same approach shows that the fast mode is generally not found in the kinetic range (Figure 4e). There are however impulsive intervals where kinetic scales are present particularly after ~0550 UT. At the lowest frequencies surveyed ($f_{SC} \lesssim 0.01$ Hz) Figure 4 shows no fast mode solutions satisfying Equation 4 exist. Wave normal angles (Figure 4f) just above these frequencies are nearly field aligned, become progressively oblique with increasing f_{SC}, and are nearly perpendicular at the largest f_{SC}. Like in the Alfvén mode, ω increases with f_{SC} but more closely approaches Ω_i at large f_{SC} (Figure 4g). Again, no clearly organized propagation direction in the plane perpendicular to $\boldsymbol{B}_o$ is found (Figure 4h).

The slow mode, like the Alfvén mode, becomes kinetic at the largest f_{SC} with wavenumbers extending well into the $k_\perp \rho_i > 1$ range (Figure 4i). Here there appears to be a background of large-scale fluctuations with impulsive intervals of highly kinetic fluctuations. The impulsive intervals coincide with enhanced spectral energy densities where analyses above the magnetometer noise floor are sometimes possible up to $f_{SC} \sim 1$ Hz. At the lowest f_{SC} the slow mode is nearly field-aligned, almost perpendicular at intermediate f_{SC}, and moderately oblique at the highest f_{SC} (Figure 4j). Wave frequencies increase with f_{SC} similar to that in the Alfvén mode (Figure 4k). The distribution of ϕ_k again indicates no clear propagation direction in the perpendicular plane (Figure 4l).

5. Discussion and Conclusion

The analyses performed above indicate that in addition to the documented Alfvénic nature of broadband electromagnetic fluctuations outside the plasmapause during storm times, a significant fraction of observed spectral energy density may also reside in fast and slow mode variations. This description provides an explanation for the compressional structures observed at large non-kinetic and intermediate scales (Chaston et al., 2012, 2015) on which the Alfvén mode is mostly transverse. These structures have the properties of diamagnetic cavities often comprising localized regions of energetic plasmas. They are decomposed in this analysis as the superposition of Alfvénic and slow mode wavelets and appear in Figure 3 at frequencies below 0.01 Hz. These Alfvénic/slow

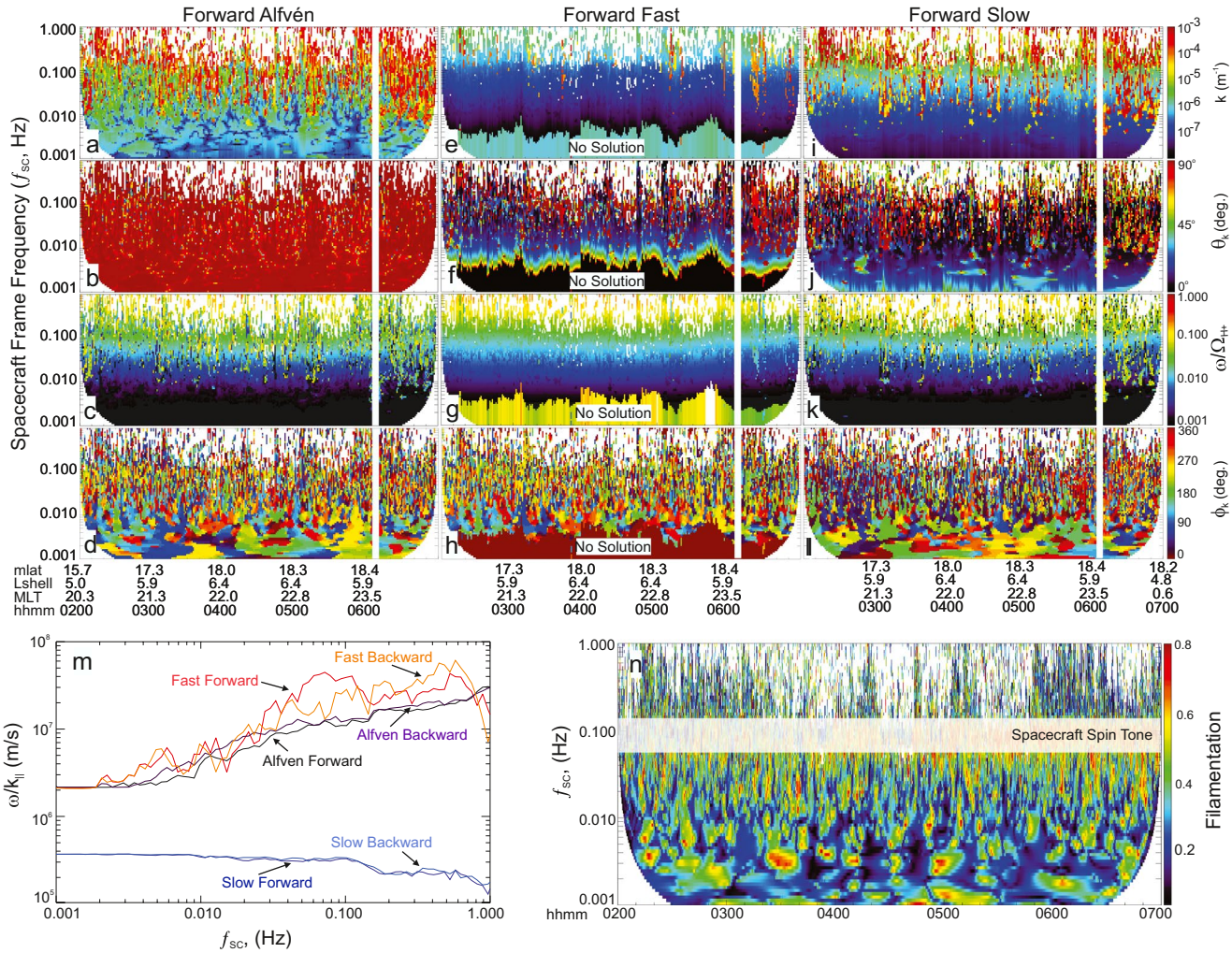

Figure 4. (a–l) Wavevector magnitude (k), Wavenormal Angle (θ_k), wave frequency normalized to the proton gyrofrequency (ω/Ω_{H+}) and azimuthal angle (ϕ_k) at minima of A_i ($\boldsymbol{k}_{SC}$) for the forward Alfvén, fast and slow modes respectively. (m) Average $\omega/k_{\|}$ of each mode as a function of f_{SC}. (n) Filamentation in the magnetic field morphology.

mode features progressively disappear after dipolarization of the geomagnetic field with reduction in slow mode composition as the spacecraft transitions to lower L-shells and passes through magnetic midnight. During this transition, the fast mode composition above 0.01 Hz intensifies.

The coexistence of spectral energy densities in all three modes is suggestive of the operation of mode coupling. This may be a consequence of inhomogeneities in the plasma (Allan & Wright, 1998, 2000; Hasegawa, 1976; Johnson et al., 2001; Lysak et al., 2009) and/or non-linear processes such as parametric decay (Chen & Zonca, 2011; Hasegawa & Chen, 1976). Figure 4m shows the average parallel phase speeds, $\omega/k_{\|}$, of each mode at minima in A_i (k_{SC}) as a function of f_{SC}. The similarity of $\omega/k_{\|}$ in the fast and Alfvén mode over much of the range shown introduces the possibility of energy transfer between these modes. While a definitive demonstration of energy transfer remains to be presented, this result suggests that such a process may have been prevalent during this storm main phase.

The lack of a distinct direction of propagation in the plane perpendicular to $\boldsymbol{B_o}$ and the broad distributions of $\overline{g_i}\,(k_\perp\rho_i, \theta_k, \phi_k)$ for the Alfvénic mode may be understood by considering the morphology of the fluctuations. Figure 4n shows the "filamentation" of the field variations in the perpendicular plane based on the relationship between the corresponding magnetic field components (Chaston, Bonnell, Wygant, et al., 2020). For planar features consistent with a single plane wave at each f_{SC} and t, the value of the filamentation should approach zero. However, Figure 4 shows the filamentation is often larger than zero, and sometimes approaches one. This

represents elliptical/filamentary features that require the superposition of modes over a range in ϕ_k to account for the associated distribution of ϵ at each f_{SC} and t. For such features there is no clearly defined direction of propagation through the plasma in the plane perpendicular to $\boldsymbol{B}_o$.

In closing, a full account of the spectral energy in the broadband electromagnetic fluctuations during the storm of 1 June 2013, requires not only a superposition of modes at each f_{SC} and t but also contributions over a range of wave-vectors in each mode. This is required by the observed non-planar field morphology and is symptomatic of the operation of the non-linear processes presumably driving the broad k-spectra. The Alfvén mode, when integrated over a range of wavevectors capable of contributing to ϑ at a particular f_{SC}, is generally the largest contributor to ϵ. However, this mode is associated with, and likely coupled to, fast and/or slow mode field variations by processes yet to be identified. While this decomposition analysis has been performed for a single storm, statistical studies of comparable events (Chaston et al., 2015, Hull et al., 2019, 2020) suggest that the properties described above are likely pervasive outside the plasmapause during geomagnetically disturbed intervals.

Data Availability Statement

Van Allen Probes measurements used in this study can be obtained from the following data repositories: EFW http://www.space.umn.edu/rbspefw-data/; EMFISIS https://emfisis.physics.uiowa.edu/data/index; HOPE/MAGEIS https://rbsp-ect.newmexicoconsortium.org/science/DataDirectories.php. High level data and numerically derived quantities used in the analysis and production of the figures can be found at https://figshare.com/articles/dataset/_/17156138. The analyses were performed using publicly available IDL based SPEDAS software (Angelopoulos et al., 2019; available at http://spedas.org/wiki/index.php?title=Downloads_and_Installation) and wavelet-based software available at http://atoc.colorado.edu/research/wavelets.

Acknowledgments
This research was supported by NASA grants NNX17AD36G, 80NSSC21K0580 and NNX17AI55G, and NSF Grant 2041971. Van Allen Probes funding is provided under NASA prime contract NAS5-01072; including the RBSP-EFW investigation and RBSP-EMFISIS investigations under JHU/APL contracts 921647, 922613, and the RBSP-ECT investigation under contract 967399. Chris Chaston thanks the Van Allen Probes team and in particular John Wygant, Geoff Reeves, Craig Kletzing and John Bonnell.

References

Allan, W., & Wright, A. N. (1998). Hydromagnetic wave propagation and coupling in a magnetotail waveguide. *Journal of Geophysical Research*, *103*(A2), 2359–2368. https://doi.org/10.1029/97ja02874

Allan, W., & Wright, A. N. (2000). Magnetotail waveguide: Fast and Alfvén waves in the plasma sheet boundary layer and lobe. *Journal of Geophysical Research*, *105*(A1), 317–328. https://doi.org/10.1029/1999JA900425

Angelopoulos, V., Chapman, J. A., Mozer, F. S., Scudder, J. D., Russell, C. T., Tsuruda, K., et al. (2002). Plasma sheet electromagnetic power generation and its dissipation along auroral field lines. *Journal of Geophysical Research*, *107*(A8). https://doi.org/10.1029/2001JA900136

Angelopoulos, V., Cruce, P., Drozdov, A., Grimes, E. W., Hatzigeorgiu, N., King, D. A., et al. (2019). The space physics environment data Analysis system (SPEDAS). *Space Science Reviews*, *215*(9), 1–46. https://doi.org/10.1007/s11214-018-0576-4

Chaston, C. C., Bonnell, J. W., Bale, S. D., Kasper, J. C., Pulupa, M., Whittlesey, P. L., et al. (2020). MHD mode composition in the inner heliosphere from the Parker Solar Probes 1st Perihelion. *The Astrophysical Journal Supplement Series*, *246*(2), 71. https://doi.org/10.3847/1538-4365/ab745c

Chaston, C. C., Bonnell, J. W., Clausen, L., & Angelopoulos, V. (2012). Correction to "Energy transport by kinetic-scale electromagnetic waves in fast plasma sheet flows". *Journal of Geophysical Research*, *117*(A12), A12205. https://doi.org/10.1029/2012JA018476

Chaston, C. C., Bonnell, J. W., Kletzing, C. A., Hospodarsky, G. B., Wygant, J. R., & Smith, C. W. (2015). Broadband low-frequency electromagnetic waves in the inner magnetosphere. *Journal of Geophysical Research: Space Physics*, *120*(10), 8603–8615. https://doi.org/10.1002/2015JA021690

Chaston, C. C., Bonnell, J. W., Wygant, J. R., Mozer, F., Bale, S. D., Kersten, K., et al. (2014). Observations of kinetic scale field line resonances. *Geophysical Research Letters*, *41*(2), 209–215. https://doi.org/10.1002/2013GL058507

Chaston, C. C., Bonnell, J. W., Wygant, J. R., Reeves, G. D., & Baker, D. N. (2020). Filamentary currents and Alfvénic vortices in the inner magnetosphere. *Geophysical Research Letters*, *47*(4), e2019GL086318. https://doi.org/10.1029/2019GL086318

Chen, L., & Zonca, F. (2011). Gyrokinetic theory of parametric decays of kinetic Alfvén waves. *Europhysics Letters*, *96*(3), 35001. https://doi.org/10.1209/0295-5075/96/35001

Cheng, C. Z., & Johnson, J. R. (1999). A kinetic-fluid model. *Journal of Geophysical Research*, *104*(A1), 413–427. https://doi.org/10.1029/1998JA900065

Cheng, C. Z., & Zaharia, S. (2004). MHD ballooning instability in the plasma sheet. *Geophysical Research Letters*, *31*(6), L06809. https://doi.org/10.1029/2003GL018823

Dombeck, J., Cattell, C., Wygant, J. R., Keiling, A., & Scudder, J. (2005). Alfvén waves and Poynting flux observed simultaneously by polar and FAST in the plasma sheet boundary layer. *Journal of Geophysical Research*, *110*(A12), A12S90. https://doi.org/10.1029/2005JA011269

Funsten, H. O., Skoug, R. M., Guthrie, A. A., MacDonald, E. A., Baldonado, J. R., Harper, R. W., et al. (2013). Helium, oxygen, proton, and electron (HOPE) mass spectrometer for the radiation belt storm Probes mission. *Space Science Reviews*, *179*(1–4), 423–484. https://doi.org/10.1007/s11214-013-9968-7

Gabrielse, C., Angelopoulos, V., Runov, A., & Turner, D. L. (2014). Statistical characteristics of particle injections throughout the equatorial magnetotail. *Journal of Geophysical Research: Space Physics*, *119*(4), 2512–2535. https://doi.org/10.1002/2013JA019638

Glassmeier, K. H., Motschmann, U., & von Stein, R. (1995). Mode recognition of MHD wave fields at incomplete dispersion measurements. *Annales Geophysicae*, *13*, 76–83.

Hasegawa, A. (1976). Particle acceleration by MHD surface wave and formation of aurora. *Journal of Geophysical Research*, *81*(28), 5083–5090. https://doi.org/10.1029/JA081i028p05083

Hasegawa, A., & Chen, L. (1976). Parametric decay of "kinetic Alfvén wave" and its application to plasma heating. *Physical Review Letters*, *36*(23), 1362–1365. Published 7 June 1976. https://doi.org/10.1103/physrevlett.36.1362

Hollweg, J. V. (1999). Kinetic Alfvén wave revisited. *Journal of Geophysical Research*, *104*(A7), 14811–14819. https://doi.org/10.1029/1998JA900132

Hull, A. J., Chaston, C. C., Bonnell, J. W., Damiano, P. A., Wygant, J. R., & Reeves, G. D. (2020). Correlations between dispersive Alfvén wave activity, electron energization, and ion outflow in the inner magnetosphere. *Geophysical Research Letters*, *47*(17), e2020GL088985. https://doi.org/10.1029/2020GL088985

Hull, A. J., Chaston, C. C., Bonnell, J. W., Wygant, J. R., Kletzing, C. A., Reeves, G. D., & Gerrard, A. (2019). Dispersive Alfvén wave control of O+ ion outflow and energy densities in the inner magnetosphere. *Geophysical Research Letters*, *46*(15), 8597–8606. https://doi.org/10.1029/2019GL083808

Jahn, J.-M., Goldstein, J., Kurth, W. S., Thaller, S., De Pascuale, S., Wygant, J., et al. (2020). Determining plasmaspheric density from the upper hybrid resonance and from the spacecraft potential: How do they compare? *Journal of Geophysical Research: Space Physics*, *125*(3), e2019JA026860. https://doi.org/10.1029/2019JA026860

Johnson, J. R., Cheng, C. Z., & Song, P. (2001). Signatures of mode conversion and kinetic Alfvén waves at the magnetopause. *Geophysical Research Letters*, *28*(2), 227–230. https://doi.org/10.1029/2000gl012048

Keiling, A., Wygant, J. R., Cattell, C., Peria, W., Parks, G., Temerin, M., et al. (2002). Correlation of Alfvén wave Poynting flux in the plasma sheet at 4–7 RE with ionospheric electron energy flux. *Journal of Geophysical Research*, *107*(A7), 1132. https://doi.org/10.1029/2001JA900140

Kepko, L., Kivelson, M. G., & Yumoto, K. (2001). Flow bursts, braking, and Pi2 pulsations. *Journal of Geophysical Research*, *106*(A2), 1903–1915. https://doi.org/10.1029/2000JA000158

Kivelson, M. G., & Russell, C. T. (Eds.), (1995). *Introduction to space physics* (p. 586). Cambridge University Press (ISBN: 0521451043).

Kletzing, C. A., Kurth, W. S., Acuna, M., MacDowall, R. J., Torbert, R. B., Averkamp, T., et al. (2013). The electric and magnetic field instrument suite and integrated science (EMFISIS) on RBSP. *Space Science Reviews*, *179*(1–4), 127–181. https://doi.org/10.1007/s11214-013-9993-6

Liu, J., Angelopoulos, V., Zhang, X.-J., Turner, D. L., Gabrielse, C., Runov, A., et al. (2016). Dipolarizing flux bundles in the cis-geosynchronous magnetosphere: Relationship between electric fields and energetic particle injections. *Journal of Geophysical Research: Space Physics*, *121*(2), 1362–1376. https://doi.org/10.1002/2015JA021691

Liu, J., Lyons, L. R., Archer, W. E., Gallardo-Lacourt, B., Nishimura, Y., Zou, Y., et al. (2018). Flow shears at the poleward boundary of omega bands observed during conjunctions of Swarm and THEMIS ASI. *Geophysical Research Letters*, *45*(3), 1218–1227. https://doi.org/10.1002/2017GL076485

Lysak, R. L., & Lotko, W. (1996). On the kinetic dispersion relation for shear Alfvén waves. *Journal of Geophysical Research*, *101*(A3), 5085–5094. https://doi.org/10.1029/95JA03712

Lysak, R. L., Song, Y., & Jones, T. W. (2009). Propagation of Alfvén waves in the magnetotail during substorms. *Annales Geophysicae*, *27*(5), 2237–2246. https://doi.org/10.5194/angeo-27-2237-2009

Malaspina, D. M., Wygant, J. R., Ergun, R. E., Reeves, G. D., Skoug, R. M., & Larsen, B. A. (2015). Electric field structures and waves at plasma boundaries in the inner magnetosphere. *Journal of Geophysical Research: Space Physics*, *120*(6), 4246–4263. https://doi.org/10.1002/2015JA021137

Miura, A., Ohtani, S., & Tamao, T. (1989). Ballooning instability and structure of diamagnetic hydromagnetic waves in a model magnetosphere. *Journal of Geophysical Research*, *94*(A11), 15231–15242. https://doi.org/10.1029/JA094iA11p15231

Motschmann, U., Glassmeier, K. H., & Pincon, J. L. (1998). Multi-spacecraft filtering: Plasma mode recognition, In G. Paschmann & P. W. Daly (Eds.), *Analysis methods for multi-spacecraft data* (p. 79). *ISSI Scientific Report SR-001* (Electronic edition 1.1), 1998, 2000 ISSI/ESA.

Moya, P. S., Pinto, V. A., Viñas, A. F., Sibeck, D. G., Kurth, W. S., Hospodarsky, G. B., & Wygant, J. R. (2015). Weak kinetic Alfvén waves turbulence during the 14 November 2012 geomagnetic storm: Van Allen Probes observations. *Journal of Geophysical Research: Space Physics*, *120*(7), 5504–5523. https://doi.org/10.1002/2014JA020281

Panov, E. V., & Pritchett, P. L. (2018). Dawnward drifting interchange heads in the Earth's magnetotail. *Geophysical Research Letters*, *45*(17), 8834–8843. https://doi.org/10.1029/2018GL078482

Panov, E. V., Sergeev, V. A., Pritchett, P. L., Coroniti, F. V., Nakamura, R., Baumjohann, W., et al. (2012). Observations of kinetic ballooning/interchange instability signatures in the magnetotail. *Geophysical Research Letters*, *39*(8), L08110. https://doi.org/10.1029/2012GL051668

Pritchett, P. L., & Coroniti, F. V. (2010). A kinetic ballooning/interchange instability in the magnetotail. *Journal of Geophysical Research*, *115*(A6), A06301. https://doi.org/10.1029/2009JA014752

Roux, A., Perraut, S., Roberts, P., Morane, A., Pedersen, A., Korth, A., et al. (1991). Plasma sheet instability related to the westward traveling surge. *Journal of Geophysical Research*, *96*(17), 697. https://doi.org/10.1029/91ja01106

Runov, A., Angelopoulos, V., Gabrielse, C., Zhou, X.-Z., Turner, D., & Plaschke, F. (2013). Electron fluxes and pitch-angle distributions at dipolarization fronts: THEMIS multipoint observations. *Journal of Geophysical Research: Space Physics*, *118*(2), 744–755. https://doi.org/10.1002/jgra.50121

Runov, A., Angelopoulos, V., Zhou, X.-Z., Zhang, X.-J., Li, S., Plaschke, F., & Bonnell, J. (2011). A THEMIS multicase study of dipolarization fronts in the magnetotail plasma sheet. *Journal of Geophysical Research*, *116*(A5), A05216. https://doi.org/10.1029/2010JA016316

Saito, M. H., Miyashita, Y., Fujimoto, M., Shinohara, I., Saito, Y., & Mukai, T. (2008). Modes and characteristics of low-frequency MHD waves in the near-Earth magnetotail prior to dipolarization: Fitting method. *Journal of Geophysical Research*, *113*(A6), A06201. https://doi.org/10.1029/2007JA012778

Santolík, O., Parrot, M., & Lefeuvre, F. (2003). Singular value decomposition methods for wave propagation analysis. *Radio Science*, *38*, 1010. https://doi.org/10.1029/2000RS002523, 1

Tian, S., Colpitts, C. A., Wygant, J. R., Cattell, C. A., Ferradas, C. P., Igl, A. B., et al. (2021). Evidence of Alfvénic poynting flux as the primary driver of auroral motion during a geomagnetic substorm. *Journal of Geophysical Research: Space Physics*, *126*(5), e2020JA029019. https://doi.org/10.1029/2020JA029019

Torrence, C., & Compo, G. P. (1998). A Practical guide to wavelet analysis. *Bulletin of the American Meteorological Society*, *79*(1), 61–78. https://doi.org/10.1175/1520-0477(1998)079<0061:apgtwa>2.0.co;2

Wang, T., Cao, J., Fu, H., Meng, X., & Dunlop, M. (2016). Compressible turbulence with slow-mode waves observed in the bursty bulk flow of plasma sheet. *Geophysical Research Letters*, *43*(5), 1854–1861. https://doi.org/10.1002/2016GL068147

Wygant, J. R., Bonnell, J. W., Goetz, K., Ergun, R. E., Mozer, F. S., Bale, S. D., et al. (2013). The electric field and waves instruments on the radiation belt storm Probes mission. *Sport Science Review*, *179*(1–4), 183–220. https://doi.org/10.1007/s11214-013-0013-7

Wygant, J. R., Keiling, A., Cattell, C. A., Johnson, M., Lysak, R. L., Temerin, M., et al. (2000). Polar spacecraft based comparisons of intense electric fields and Poynting flux near and within the plasma sheet-tail lobe boundary to UVI images: An energy source for the aurora. *Journal of Geophysical Research*, *105*(A8), 18675–18692. https://doi.org/10.1029/1999JA900500